HHS Public Access

Author manuscript

J Inorg Biochem. Author manuscript; available in PMC 2024 July 01.

Published in final edited form as:

J Inorg Biochem. 2023 July ; 244: 112211. doi:10.1016/j.jinorgbio.2023.112211.

Nanodisc-embedded Cytochrome P450 P3A4 Binds Diverse Ligands by Distributing Conformational Dynamics to its Flexible Elements

Lorela Paço[1], **John C. Hackett**[2], **William M. Atkins**[1]

[1]Department of Medicinal Chemistry University of Washington Seattle, WA 98195-7610

[2]Department of Chemistry and Biochemistry Florida International University Miami, FL 33199

Graphical Abstract

Author_statement

Conceptualization, William Akins, Lorela Paco, John Hackett; Data curation, John Hackett, Lorela Paco; Formal analysis, Lorela Paco, John Hackett, William Atkins; Funding acquisition, William Atkins, John Hackett; Investigation, Loreal Paco, John Hackett; Methodology, Lorela Paco, John Hackett; Project administration, William Atkins; Resources, William Atkins,John Hackett; Supervision, William atkins, John Hackett; Visualization, Lorela Paco, John Hackett; Roles/Writing - original draft, Lorela Paco; Writing - review & editing, John Atkins, William Atkins.

Declaration of interests

The authors declare that they have no known competing financial interests or personal relationships that could have appeared to influence the work reported in this paper.

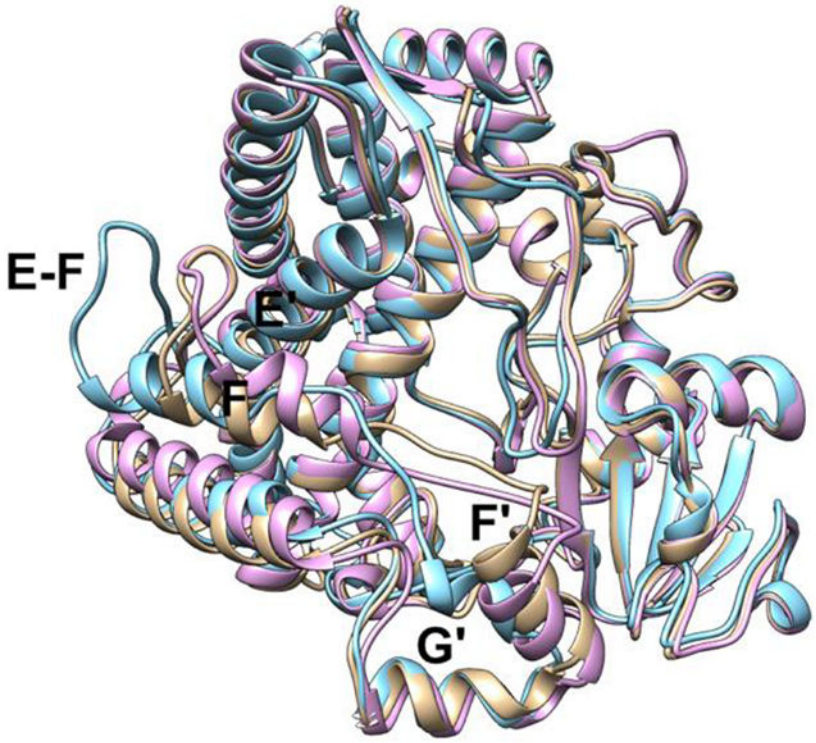

Superimposition of average structures of CYP3A4 from GaMD simulations of the ligand-free CYP3A4 (tan), CYP3A4-Azimulin complex (blue), and CYP3A4-Ritonavir complex (pink) illustrating the differences in the packing of the F-helix and E-F loop against the E-helix. MD and H/DX mass spectrometry confirm regions uniquely or universally affected by various ligands.

Introduction

CYP3A4 is a major detoxification enzyme, transforming nearly half of small molecule drugs that undergo oxidative metabolism [1]. CYP3A4 also plays a major role in mediating drug-drug interactions, and as a result, is a critical consideration in drug design and development. Despite the availability of various X-ray structures, it has been challenging to predict metabolism of drugs by CYP3A4 due to its extreme ligand promiscuity that may be affected by many factors including the oligomeric state of CYP3A4 [2], [3], the presence or absence of redox partners [4], membrane composition [5]–[7], and co-solvent conditions [8], [9]. Each of these factors also affects the well-established homotropic and heterotropic allosteric properties of CYP3A4 that are also promiscuous and enigmatic [10].

One frequently suggested mechanism by which proteins achieve substrate promiscuity is with their conformational ‘flexibility’ [11]. CYP3A4 has long been described as a flexible enzyme with a large hydrophobic active site that can accommodate multiple ligands and multiple ligand orientations [12]–[14]. Evidence for the flexibility of the enzyme primarily stems from crystal structures of CYP3A4 bound to various ligands showing large local deviations from the free structure that vary in direction and magnitude. The expanding collection of P450 crystal structures has revealed that significant local rearrangements in the

presence of ligands are not unique to CYP3A4, and P450s of varying substrate selectivity have been shown to adopt diverse conformations [15]–[19], prompting a need for a more rigorous assessment of the role of conformational flexibility in promiscuous interactions with ligands. Beyond static structures, our understanding of the dynamic properties of CYP3A4 has been obtained primarily from X-ray crystallography, computational, and spectroscopic studies with selected ligands and the range of ligand-dependent effects on the backbone dynamics is not established [20]–[29].

Previously, our laboratory has used hydrogen-deuterium exchange mass spectrometry (HDX-MS) to analyze dynamics of CYP3A4 incorporated in lipid nanodiscs with a type II inhibitor, ketoconazole, and a type I allosteric substrate, midazolam [22], [26]. HDX refers to the exchange reaction of backbone amide hydrogens with deuterium from solution. When coupled with sensitive detection methods such as NMR or MS, HDX reports on the accessibility of amide hydrogens and provides insights into the conformational dynamics of proteins in different states [30], [31]. Ketoconazole and midazolam had distinct effects on CYP3A4 dynamics and in both cases the HDX effects were globally distributed. Notably, some protein regions were affected by both ligands, whereas others were uniquely affected by either ketoconazole or midazolam. Based on the complex global responses, we postulated that some dynamic responses of CYP3A4 are essential for all ligand binding, while others are ligand dependent.

Here, we combine HDX-MS with Gaussian Accelerated Molecular Dynamics Simulations (GaMD) to report the effects of six ligands on the conformational dynamics of CYP3A4 embedded in POPC lipid nanodiscs (NDs). Ligands were selected to represent a range of chemical structures and functions to reflect the vast pool of CYP3A4-ligand interactions, including ligands for which crystal structures are available for the bound complexes to compare with behavior in a membrane. The ligands studied were ritonavir (RIT), nifedipine (NIF), bromoergocriptine (BEC), miconazole (MIC), azamulin (AZA) and testosterone (TST) (Figure 1; Table 1). RIT is an HIV protease inhibitor and potent CYP3A4 inactivator [32–34]. NIF is a calcium channel blocker used as an antihypertensive drug that is also a marker substrate of CYP3A4 metabolism [35]. BEC is a dopamine receptor agonist that acts as substrate and inhibitor of CYP3A4 [36,37]. MIC is an azole antifungal drug and inhibitor [20]. AZA is a pleuromutilin antibiotic and suicide substrate of CYP3A4 that was discontinued after Phase I trials due to potent CYP3A inhibition [38,39]. Lastly, TST is a well-characterized marker substrate and allosteric effector of CYP3A4 [40,41]. With these ligands we performed a correlational analysis of HDX affects to screen for ligand-mediated correlated motions in CYP3A4. GaMD and principal component analyses were performed with RIT and AZA complexes only and compared to the ligand-free enzyme.

Methods

Materials and chemicals

Reagents were purchased from Sigma or Fisher unless otherwise stated. RIT and BEC were obtained from Apexbio and Santa Cruz, respectively. Deuterium oxide “100%” was obtained from Cambridge Isotope Laboratories. Solvents for LC-MS/MS were Optima LC/MS grade, other water used was from a Barnstead nanopure UV dispenser.

CYP3A4 and MSP1D1 expression and purification

Recombinant CYP3A4 and MSP1D1(−) were expressed and purified as previously described [22], [42–45]. *E. coli* C41(DE3) cells were transformed with a pCWori+ vector encoding genes for the Nf14 CYP3A4 construct and ampicillin resistance. The Nf14 construct has a N-terminal Δ3–11 deletion and a C-terminal 5xHis tag [46]. Following expression, cells were centrifuged at 6,650 × g at 4°C for 30 min, and pellets were stored at −80°C until purification. The purification steps were carried out in the dark at 0–4°C with pH 7.4 buffers. β-Mercaptoethanol (βME), TST, and non-ionic detergents were added immediately before use. Cell pellets were gently resuspended in lysis buffer (20 % (v/v) glycerol, 100 mM KPi, 10 mM βME, 100 μM TST, 3% (v/v) Emulgen 913, 20 mM imidazole) supplemented with 2 mg/ml lysozyme, 10 μl/ml protease inhibitor cocktail for His-tagged proteins and 0.1 μl/ml benzonase nuclease. Resuspended cells were stirred for 1 hr, passed twice through a handheld Potter-Elvehjem homogenizer, and stirred for an additional 4 hrs. After ultracentrifugation at 100,000 × g for 1 hr, the supernatant was loaded overnight onto a ~30 ml His60 Ni Superflow (Clontech) column pre-equilibrated with wash buffer 1. Following washing with 8–10 column volumes (CVs) of wash 1 (20% glycerol (v/v), 50 mM KP_i, 2 mM βME, 50 μM TST, 0.2%(v/v) Anapoe $C_{12}E_{10}$, 300 mM KCl, 20 mM imidazole [IMZ]), 8–10 CVs of wash 2 (20% (v/v) glycerol, 50 mM KP_i, 2 mM βME, 50 μM TST, 0.1% (w/v) sodium cholate, 300 mM KCl, 20 mM IMZ, 100 mM glycine), and 20 CVs of wash 3 (20% glycerol, 50 mM KP_i, 2 mM βME, 50 μM TST, 0.1% (w/v) sodium cholate, 40 mM IMZ), CYP3A4 fractions were eluted with a linear IMZ gradient (20% glycerol, 25 mM KP_i, 2 mM βME, 50 μM TST, 0.1% sodium cholate, 50–500 mM IMZ). Red fractions were diluted 1:1 with a cold solution of 20% glycerol and 0.1% cholate to lower the concentration of KP_i before loading onto a ~25 ml hydroxyapatite (HA) column pre-equilibrated with 20% glycerol, 10 mM KP_i, 0.1% sodium cholate, and 2 mM βME. After washing the HA column with 20 CVs of 20% glycerol, 25 mM KP_i, and 2 mM βME, CYP3A4 fractions were eluted with 20% glycerol, 400 mM KP_i, and 2 mM βME. Fractions were analyzed via SDS-PAGE, pooled accordingly, and dialyzed into CYP3A4 storage buffer (100 mM KP_i, 20% glycerol, 0.5 mM tris-carboxyethylphosphine (TCEP), 1 mM EDTA). The protein concentration was determined by measuring the difference in absorbance between the CO-bound ferrous (reduced) CYP3A4 and unbound ferrous CYP3A4 as follows: $\Delta Abs_{(450\ nm - 490\ nm)}$ of Fe^{2+}:CO – $\Delta Abs_{(450\ nm - 490\ nm)}$ of Fe^{2+} = $\Delta\varepsilon_{450\ nm - 490\ nm}$ *b*c, where $\varepsilon_{450\ nm - 490\ nm}$ = 91 mM^{-1} cm^{-1} [47]. No P420 was detected based on the absorbance at 420 nm.

E. coli BL21-Gold (DE3) cells were transformed with a pET vector encoding genes for MSP1D1 and kanamycin resistance. Cells were harvested at 6,650 × g at 4 °C for 15 min. Purification steps were carried out at 4°C. Cell pellets were resuspended in lysis buffer (20 mM KP_i, pH 7.4, 1% Triton X-100) supplemented with 2 mg/ml lysozyme, 10 μl/ml protease inhibitor cocktail, 0.1 μl/ml benzonase nuclease, and lysed twice with a French Press. After ultracentrifugation for 45 min at 45,000 ×g, the supernatant was loaded overnight onto a ~25 ml His60 Superflow Ni column pre-equilibrated with wash buffer 1 (40 mM Tris, pH 8.0, 300 mM NaCl, 1% Triton X-100). Following washing with 5–7 CVs of wash buffer 1, 5 CVs of wash buffer 2 (40 mM Tris, pH 8.0, 300 mM NaCl, 50 mM cholate, 20 mM IMZ), 5 CVs of wash buffer 3 (40 mM Tris, pH 8.0, 300 mM NaCl, 50

mM IMZ), MSP1D1 was eluted with a linear IMZ gradient (40 mM Tris, pH 7.4, 300 mM NaCl, 40–400 mM IMZ). MSP1D1 containing fractions were pooled, concentrated, and dialyzed into MSP1D1 storage buffer (20 mM Tris, pH 7.4, 100 mM NaCl, 0.5 mM EDTA). The MSP1D1 concentration was spectrally determined using the extinction coefficient of 21 mM^{-1} cm^{-1} [45].

The His tag of MSP1D1 was cleaved to yield MSP1D1(−) as previously described [26, 29]. Following the cleavage reaction with Pro-TEV Plus Protease (Promega), the reaction mix was filtered through a 0.2 μm filter and buffer exchanged into column running buffer (40 mM Tris, pH 8.0, 300 mM NaCl, 50 mM cholate), before loading onto a ~8 ml His60 Superflow Ni column pre-equilibrated with running buffer, collecting the flowthrough. After washing with 3 CVs of running buffer, the combined flowthrough with MSP1D1 (−) was buffer-exchanged into storage buffer (40 mM Tris, pH 8.0, 300 mM NaCl), concentrated to ~150 μM and stored at −80°C until ND preparation. The pure MSP1D1(−) was characterized via SDS-PAGE and the concentration was spectrally determined using the extinction coefficient of 18.2 mM^{-1} cm^{-1} [45].

Nanodisc preparation

CYP3A4-NDs containing POPC were prepared as previously described with few modifications [22], [26], [45]. Briefly, POPC powder (Avanti Polar Lipids) was dissolved in chloroform (~2 g/ml) and the concentration of phospholipids was determined by measuring the total phosphorous [45]. To make the lipid film, POPC chloroform stock was placed under a gentle N_2 stream in a glass tube while twirling the tube at an angle until a thin layer of film was formed. The film was dried overnight in a vacuum desiccator to remove traces of chloroform and solubilized in cholate by intermittent sonicating, low heat, and vortexing, until the solution was clear. In the meantime, CYP3A4 was treated with 0.1 % Emulgen 911, and left to nutate in the dark at RT for 1 hr, before exchanging into disc-forming buffer (DFB; 100 mM KP_i, 50 mM NaCl, pH 7.4) supplemented with 0.1% Emulgen 911. To prepare the ND reaction mix, cholate-solubilized lipids, MSP1D1(−) and CYP3A4 were mixed in an empirically determined ratio (55:1:0.1). More cholate and DFB were added for a final 3:1 cholate: lipid ratio. The reaction mix was rotated at 4 °C for 1 hr and transferred to 2 × 10 ml capped centrifuge columns (Pierce) containing 1 g/ml pre-rinsed Amberlite XAD-2 beads to initiate the nanodisc assembly. The disc and beads mixtures were gently rotated at 4 °C for 6 hrs. To separate the NDs from the beads, the columns were uncapped and spun down at low speed inside 50 ml Falcon tubes. The beads were rinsed twice with DFB and the collected flowthrough containing the NDs was filtered with a 0.2 μm filter. To remove leftover detergents, NDs were dialyzed three times against 1 L of DFB with 2 mM βME (2 × 1 hr, overnight) before loading onto a 5 ml His60 Ni Superflow column pre-equilibrated with DFB. After washing with 3–5 CVs of DFB and 3–5 CVs of DFB+20 mM IMZ, red fractions were eluted with DFB+300 mM IMZ, and concentrated to 8–9 ml before injecting into a Superdex 200 10/300 GL column pre-equilibrated with DFB+2 mM βME for further purification by SEC. The pure fractions were combined, exchanged into DFB+10% glycerol, concentrated to ~10 μM and stored at −80°C. The concentration and P420 content were spectrally determined as described for CYP3A4. No P420 was detected.

HDX sample preparation

HDX was performed as previously described [22], [48] with six ligands in two groups: (I) RIT, NIF, and BEC, and (II) MIC, AZA and TST. Ligand-free samples were included in each group. Free or bound CYP3A4-NDs were exchanged at 24°C for 30 s, 5 m, and 90 m in duplicate, in random order. Undeuterated control samples were prepared in deuterium-free buffer. Details of the HDX reactions are reported in SI Tables 1 and 2. To initiate the exchange reaction, a 10 μl aliquot of free or bound CYP3A4-NDs, pre-incubated at 24°C for 30 min, was mixed with 90 μl of deuterated HDX buffer (50 mM HEPES, pH 7.0, 50 mM NaCl, 2 mM TCEP). The concentration of ligands and CYP3A4-NDs in the 100 μl HDX sample were ~20× their reported K_D values (predicted bound fraction >90%) and 0.9 −1.2 μM, respectively. Final deuterium content was 83.2%. The exchanged sample was quenched with 100 μl of ice-cold quench solution (1.2% formic acid and 0.4% TFA) and transferred to pre-rinsed immobilized pepsin beads (Pierce) on ice. To prepare the beads, a 200 μl aliquot of 1:1 pepsin slurry was spun at 14,000 ×g for 30 s in a chilled microcentrifuge. After discarding the liquid, 400 μl of 0.8% FA was added to the beads and the slurry was centrifuged for another 30 s. The supernatant was decanted, and the rinsed beads were returned on ice. 4.2 μl of 250 mM cholate in HDX buffer was added to the cap of the pepsin tube. The quenched sample was digested on ice for 5 min with rapid vortexing every 30 s. At 4 min, 10 μl of 300 mg/ml ZrO_2-coated silica resin beads in 0.8% FA was added to facilitate POPC removal. At 5 min, the mix was transferred to a 2 ml centrifuge tube filter (Corning, pore size 0.45 μm) and centrifuged at 14,000 ×g for 30 s. 200 μl of flowthrough was rapidly transferred, flash frozen in LN_2, and stored at −80°C until MS analysis.

HDX Mass Spectrometry

Samples were thawed on ice for 5 min and at room temperature for 80–100 s before injecting into an in-house mobile LC system kept at 1°C [49]. Peptides were loaded onto a BEH Shield RP18 Vanguard trap column (Waters, 1.7 μm particle size, 2.1 × 5 mm) by flowing loading buffer (0.1% FA, 0.025% TFA in water) at 200 μl/min for 5 min and then separated on a Hypersil GOLD C_{18} column (1.9 μm particle size, 50 × 1.0 mm) at 40 μl/min for 10 min using a 2–50% gradient of solvent B (A: 2% CH_3CN, 0.1% FA, 0.025% TFA in water; B: 0.1% FA in CH_3CN). To minimize carry-over, the syringe, LC lines, and columns were extensively washed as previously described [50]. C_{18}-separated peptides were directed to a Waters Synapt G2-Si Q-TOF mass spectrometer with ion-mobility enabled for MS analysis. Source and StepWave ion guide settings were adjusted to minimize gas-phase deuterium loss [51]. A Thermo LTQ-Orbitrap (resolution 60,000) was used to analyze undeuterated samples by MS/MS.

HDX and correlation analysis

Peptide assignments were made using MS^E data with PLGS Version 3 and MS/MS data with Protein Prospector [22] from undeuterated samples. Retention and drift times were identified with Drift Scope 2.0. HX-Express v2 was used to analyze and summarize deuterium uptake of peptides by binomial fitting of the raw spectra [51]. Multiple charge states and overlapping peptides were analyzed and manually curated to exclude noisy or hard to separate peptides. ΔHDX values were calculated by subtracting the deuterium uptake of

peptides in the free state from the bound state. Fully deuterated samples were not obtained due to the primary goal of the study being to compare different bound states of CYP3A4. A statistical threshold for a significant difference in HDX between two states was calculated in the form of a 95% confidence interval (CI) based on the average standard deviation [52].

Heatmap of correlation matrix of the sum ΔHDX for peptides in different bound states was generated in GraphPad Prism 9 using the correlation matrix analysis tool to compute Pearson correlation coefficients. Two-tailed p values were used to assess confidence. A Bonferroni correction was used to correct the standard p value of 0.05 to account for multiple comparisons (0.05/number of pairwise comparisons). Peptides that were not significantly affected according to the significance thresholds established in the HDX analysis were excluded to avoid false positives. The chiclet plot was manually constructed in PowerPoint (2021). Protein structures were generated in PyMOL 2.5.

Molecular Dynamics Simulations

Crystal structures of ligand-free CYP3A4 (PDB ID: 1TQN) [13] as well as those bound to RIT (PDB ID: 3NXU) [37], and AZA (PDB ID:6OOA) [42] were used as the initial structures for MD simulations. To match the CYP3A4 sequence in the simulations to that of the protein used in HDX-MS measurements, the truncated N-terminus of the Nf14 construct and C-terminal His-tag were appended to each structure. Internal stretches of amino acids missing from the structures were added with Modeller [53]. The initial orientations of CYP3A4 in the membranes were estimated using the Positioning of Proteins in Membranes (PPM) web server [54]. CYP3A4 and ligand complexes were then inserted into a 120 Å × 120 Å POPC bilayer, solvated with TIP3P water, and 0.15 M NaCl was added to ensure electrical neutrality using CHARMM-GUI[55]. The initial height of the periodic systems was approximately 140 Å. The components of each simulation are listed in Supporting Table S1. All MD simulations were performed using NAMD 2.14 [56] and the CHARMM36 [57] force field for all components except the ligands, which were described by the CGenFF [58]. NBFIX parameters were applied to describe interactions between Na^+ ions and amino acid carboxylates. Parameters for histidine imidazole ligation to heme were mapped onto the thiazole-heme interaction to describe cooridination of this ligand to the heme. These parameters are summarized in Table S2. All simulations were performed in the NPT ensemble at 298.15 K using periodic boundary conditions with flexible cell dimensions and constant area for the membrane bilayer. Langevin dynamics were used for constant temperature constant temperature control, using a damping coefficient of 0.5 ps^{-1}. Constant pressure control was achieved using the Nose'-Hoover Langevin piston method [59], [60] with a target pressure of 1.01325 bar,a barostat oscillation time scale of 50 fs, and a barostat damping time scale of 25 fs. A 12 Å cut off was used for both electrostatic and van der Waals calculations. Bonds to hydrogen were restrained with the ShakeH algorithm and a 2 fs time step was used. All systems were initially minimized for 10,000 steps and followed by a 4 ns equilibration of the lipids, water, and ions with the coordinates of the protein and ligands frozen. This was followed by a subsequent 4 ns equilibration of the entire system with the protein C_α atoms restrained to their initial positions by a harmonic constraint of 5 kcal mol^{-1} $Å^{-2}$. After completion of the preparative simulations, the systems were equilibrated for an additional 100 ns. Finally, a 50 ns simulation was performed to collect

the potential statistics (V_{min}, V_{max}, V_{avg}, and σ_V) necessary to calculate the boost potential for Gaussian-accelerated molecular dynamics (GaMD) simulations [61], [62]. The endpoint of each preparatory GaMD simulation was used to successively run four simulations with durations of 0.43 μs, 0.40 μs, and 0.42 μs for the ligand-free enzyme, for the complex with AZA, and for the complex with RIT, respectively, with independently randomized velocities at 298.15 K. GaMD simulations were performed in "dual-boost" mode, meaning that boost potentials were added to both the dihedral and total system potential energies by setting the reference energy to the lower bound, $E = V_{max}$. The upper limit for the dihedral and total boost potential energies was set to 6 kcal mol^{-1} (~$10k_BT$). Trajectory frames were saved every ns, although the initial ~100 ns of each of the four GaMD runs was excluded from the analyses.

Principal component analyses (PCA) were performed on trajectories reduced to their backbone C, O, N and C_α atoms with MATLAB R2022a by eigenvalue decomposition. To avoid skewing the characteristics of the lowest modes with the extensive fluctuations of the N- and C-termini, including the histidine tag, analyses were restricted to folded protein core including residues 32 to 496. Rotational and translational degrees of freedom were removed by superimposing trajectory snapshots and minimizing the root mean square deviation between atomic positions compared to an average structure using MDToolbox [63]. So-called temperature factors (B_i) for the i^{th} normal mode were calculated using $B_i = \frac{8\pi}{3} X_i W_i$ where X_i and W_i are the normal modes (eigenvectors) and the square roots of the variances (eigenvalues) derived from PCA, respectively. Fluctuations associated with each normal mode were illustrated by propagating the atomic coordinates of the average structures by $csin\theta\, X_i W_i$ over $[0,2\pi]$ in ten equally spaced increments. c is a scaling factor to aid visualization.

Ensemble averaged solvent accessible surface areas for backbone N-H atoms were calculated using FreeSASA [64] with the algorithm of Lee and Richards [65] and atomic radii from Tsai and coworkers using all protein, heme and ligand atoms from the concatenated GaMD trajectories [66].

Results

HDX-MS was performed with CYP3A4-NDs mixed with co-solvent or six ligands: RIT, BEC, NIF, MIC, AZA, and TST. The 30 s – 90 m HDX reaction time course was chosen based on previous work and preliminary data corrected for back-exchange of the deuterium label showing that HDX proceeds to >70% for most peptides within 90 m (unpublished). Relative deuterium uptake is reported for 65 peptides that cover 89.3% of the Δ(3–11)-CYP3A4 sequence or 79.4% of the backbone amide hydrogens. The first two residues of each peptide quickly back-exchange the deuterium label and are not detectable by HDX [67]. Uncovered regions include the N-anchor-A" loop and parts of the buried I and L-helices. The differences in the relative deuterium uptake of the bound and free states are summarized in Figure 2. Effects of ligands on CYP3A4 dynamics are globally distributed in the flexible connecting elements between the stretches of secondary structure. All the ligands affect the F-G, and to a lesser extent, the C-D and H-I-loop regions of the protein,

suggesting that backbone fluctuations in these regions play a key role in accommodating the different ligands as suggested in part by the static crystal structures.

CYP3A4 ligands increase dynamics of the F-helix

The most common ligand-induced change is an *increase* in HDX or deprotection in the E-F-F' region (peptide 193–213) (Figures 2, 3). This peptide is part of the flexible F-G cassette and contains part of the F-F' loop that, along with G-G' loop, form the 'lid' of the active site and play a key role in accommodating diverse ligands in the binding pocket. The extent to which the F-helix peptide is affected by HDX is ligand-dependent, with AZA inducing the largest deprotection and RIT the smallest. In a recent HDX analysis by Ducharme *et al* of CYP3A4 in solution, the E-helix peptide 182–189 was one of the most protected peptides when CYP3A4 was bound to either CPR or ligands [23]. In the present work, the E-helix peptide undergoes very slow exchange until the 90 m time point (0.9 Da, Figure S1), whereas it appears to exchange faster in the Ducharme analysis (~1.5 Da). In a comparison of CYP3A4 in solution and in NDs, Treuheit *et al* reported that the exchange profiles were similar for most peptides, except for the E-F-G region which exchanged more slowly in the ND-embedded CYP3A4 than in solution [22]. Thus, the E-helix is likely in a different conformation when CYP3A4 is in a membrane environment. Interestingly, various naturally occurring single nucleotide polymorphisms are concentrated on the E-helix [68], [69] and it is known to adopt a different conformation in differentially expressed CYP3A4 [70].

On the other hand, the C-terminal half of the G-helix (peptide 249–261) has *decreased* HDX or is protected with type II ligands RIT and MIC causing the largest protection, and AZA the smallest (Figures 2, 3). The G-helix was also strongly protected with ketoconazole, another type II ligand [22]. Exchange profiles from overlapping peptides 249–271 and 262–271 (Figure S1) indicate that the difference in HDX is in the 251–263 portion of the G-helix since HDX of peptide 262–271 (G-H loop) is not significantly altered in the ligand-bound complexes.

Another commonly affected region is the C-terminal half of the C-helix (Figures 2,3). Overlapping peptides 126–133 and 126–137 (Figure S1) show that the reported HDX difference is mainly due to the 133–137 portion of the C-helix that connects to the neighboring D-helix. The N-terminal half of the C-helix (peptide 126–133) and the preceding B'-C loop (peptide 114–125) that makes contacts with ligands in the active site exchange deuterium poorly. The B'-C loop is also characterized by lower-than-average B-factors in the crystal structures (Figure S2). It is possible that the changes observed at the C-D region are propagated there via movements of the C-helix or B-C loop in the active site.

Lastly, the H-I loop region (peptide 275–292) is deprotected by all ligands in the early time points of the exchange reaction (Figures 2,3). The H-I loop is highly flexible and not fully resolved in any of the CYP3A4 crystal structures. It is likely that changes are propagated at this loop via the N-terminus of the I-helix which is known to 'bend' or locally distort in structures with different ligands.

Except for the F-helix peptide that contains a portion of the F-F' loop, the ligand-mediated HDX effects on CYP3A4 are not localized in the active site (Figure 3). Four of the five peptides commonly affected by ligands are in PR4 (as originally defined for the CYP2 enzymes; residues 203–298 [71]. They all flank substrate recognition sites and have among the highest B-factors in available crystal structures (Figure S2). Several peptides in the B/C and F/G motifs contain gate-keeper residues that border multiple ingress/egress channels [72]. Though HDX does not capture pre-equilibrium events such as transient opening/closing of substrate channels, structural plasticity of such elements may impact substrate selectivity and binding modes at equilibrium [20], [73]. Collectively, the results suggest that the F-helix, G-helix, H-I loop, and C-D region act as "adjustable straps" that tailor their conformation in response to disrupting events in the protein environment to maintain their relative packing.

Unique HDX effects are dominant in the ligand binding site.

Peptides that are significantly affected by only one of the ligands studied are typically located in the active site between the heme and membrane-interface (Figure 3), likely reflecting differences in the specific binding mode of each ligand. For instance, AZA causes the deprotection of several peptides spanning the F'-G'-G region (Figures 2, 3) as expected based on a crystallographic model that showed little deviation from the free state except for the disordering of the F'-helix due to a steric clash of AZA with the F-F' loop [42]. Consequently, the F-F' loop does not seal the active site and is exposed to the bulk solvent. Here, the F'-G' motif is deprotected by AZA suggesting that the F'-helix is indeed partially disordered in near-native conditions.

Other uniquely affected peptides are found in the B-C loop that contains the long B-B' loop, B'-helix and shorter B'-C loop. The region is part of PR2 [74] and contains the functionally important Ser119 residue which is known to make side chain-mediated contacts with ligands in the active site and helps dictate their final conformation in the bound complex [27], [75]. In CYP3A4, PR2 is not flexible and is characterized by medium-low B-factors in the crystal structures and medium-low exchange in our HDX analysis. Peptides 114–122 and 114–125 that contain the B'-C loop exchange slowly for all the ligands but MIC. Additionally, the exchange profiles in the MIC-bound complex appear bimodal, indicating at least two conformations of the B'-C loop when MIC is bound. (Figure S3).

The longer B-B' loop (peptide 103–113) is modestly protected from exchange with BEC (Figure 3). Despite its large size, BEC fits in the active site without significantly affecting the backbone configuration of CYP3A4. The crystal structure of the bound complex is almost identical to that of the free enzyme (C_α RMSD= 0.29 Å) [40]. Similarly, the HDX data show modest changes in the BEC complex. The protection of the B-B' loop may be due to an orthosteric interaction with the indole end of BEC that extends towards the loop. It should be emphasized that the B-B' loop readily exchanges deuterium, yet is minimally affected by most ligands, suggesting that the backbone of the B-B' loop does not significantly change conformation in the presence of ligands.

Peptides 34–51 and 34–52 that contain the A"-A' loop and part of the A'-helix are the only peptides that, depending on the ligand, are either protected (RIT, BEC), deprotected (AZA),

or not significantly affected (NIF, MIC and TST). (Figures 2,3). The loop is part of PR1 which in CYP3A4 is not flexible [21] and is characterized by medium-low B-factors. In our HDX analysis the loop is dynamic and readily exchanges with deuterium. The dynamics of the loop are likely linked to the neighboring A'-A turn motif that contributes to contacts with larger ligands in the active site. In the case of AZA, where such contacts are absent as AZA points away from the A'-A turn in the crystal structure, the deprotection of A"-A' loop may be due to the increased disorder and solvent exposure at the F'-G' motif upon AZA binding as discussed above. Finally, MD simulations of full-length CYP3A4, place the A"-A' loop in the membrane [76], [77]. It is therefore likely that the dynamics of this region are sensitive to the surrounding lipid environment and the partitioning of hydrophobic ligands between the membrane and protein domains.

Modest ligand-dependent differences are observed in the K-β1 loop (peptide 364–371), C-terminus loop (471–491) in the active site, the D-E region (peptides 138–151, 157–176), J-J' loop (337–351), and proximal loop near the heme (429–444). The protection at the K-β1 loop is likely due to orthosteric contacts with ligands in the active site. The HDX effect of ligands at this site is likely underestimated due to the 364–371 peptide exchanging poorly.

Correlated motions of the G-helix and C-D region.

To determine whether correlated motions are present in ligand-bound CYP3A4, we performed a correlation analysis of the sum of differences in deuterium uptake at 30 s, 5 m, and 90 m for the peptides that were significantly affected by ligands. To avoid false positives, correlation factors for peptides that were affected by at least 5 ligands are reported. As expected, overlapping peptides (157–176 and 157–178, 190–213 and 193–213, 249–261 and 249–271) showed the strongest correlation (Figure 4A). More interestingly, there is a strong correlation between non-overlapping peptides in the G-helix (peptide 249–261) and the C-D region (peptide 126–137) (Figure 4A–C). Despite being more than 13 Å apart, the strong protection at the G-helix correlates well with deprotection of the C-D region (R^2=0.91, p = 0.0033). The 'anti-correlation' is most pronounced with type II ligands RIT and MIC, but other ligands including previously published ketoconazole [22] and midazolam [26] follow this trend. This anti-correlation indicates that the ligands that protect peptide 249–261 the most, do so at the expense of deprotection of peptide 126–137, and vice-versa.

Molecular dynamics simulations.—The ligand-free enzyme, AZA, and RIT complexes were selected for molecular dynamics (MD) simulations to guide interpretation of the observations made in the HDX-MS experiments. In addition to being representative type I and type-II ligands, AZA and RIT represent the extremes of deprotection and protection from HDX. MD simulations support that these ligands induce dramatic but distinct changes in the flexible regions of CYP3A4. Differences in the residue-wise root mean square fluctuations (RMSFs) (Figure S4) show that AZA induces large increases in protein mobility, most notably in the E-F loop, F-F', and G' regions. In the case of RIT, the increases in mobility are largely restricted to the H-I, K-K', and K"-L regions, with apparent suppression of motion in the G-H loop. While the RIT's binding mode in the membrane associated CYP3A4 evaluated herein resembles that in the crystal structure, two binding

modes were observed for AZA in the simulations (Figure S5). Both maintain a similar positioning of the pleuromutilin core above the heme that is consistent with the crystal structure, although the orientation of the thioaminotriazole chain adopts two conformations. The minor binding mode (19% of trajectory) resembles that observed in the crystal structure with the thioaminotriazole group oriented toward the disordered F-F' loop (residues 211–217). The novel, predominant AZA binding mode (81% of trajectory) sandwiches the thioaminotriaziole between the hairpin intervening between the β_3 strands and the stretch of amino acids linking the K helix and the third strand of β_1. This binding mode is apparently stabilized by hydrogen bonds between the thioaminotriaziole group and the backbone of Ile369 and Leu483.

Features of the conformational changes that contribute significantly to protein function are captured by the lowest frequency normal modes. Perturbation of the vibrational manifold and the characteristics of the associated modes, such as by ligand binding, modulate protein function. To the extent that conformational fluctuations lead to variations in hydrogen bonding and/or solvent exposure of backbone amides, such motions are susceptible to interrogation by HDX-MS. Decomposition of an MD-derived conformational ensemble into a set of orthonormal modes by PCA highlights the most statistically-relevant large scale conformational changes from the ensemble, also known as the essential dynamics [78]. GaMD were used to generate four ~0.45 μs trajectories each for ligand-free as well as the AZA and RIT CYP3A4 complexes. Scree plots, illustrated in Figure S6, show the characteristic 'kink' at the fifth mode, representing 42%, 50%, and 54% of the total variance in the respective trajectories. Propagation of the GaMD-derived average structure along each of the first three modes of the ligand-free, AZ-, and RIT-CYP3A4 complexes are illustrated in Figure 5. Propagation along the fourth and fifth modes as well as composite of the first five modes are illustrated in Figure S7. The lowest frequency normal modes are dominated by motions of CYP3A4 flexible elements, although there are distinct differences between the three ligand bound states that parallel observations made in the HDX-MS measurements. Motion in the lowest frequency normal modes of ligand-free CYP3A4 are localized to regions of the protein observed to directly contact ligands, those putatively involved in harvesting ligands from the membrane [24], and regions distant from the active site but nevertheless expected to be flexible. 'Temperature factors' for ligand-free CYP3A4 and differences between ligated and ligand-free CYP3A4 are illustrated in Figure 6. A direct correlation between the rate and extent of HDX and the calculated temperature factors should not be expected, as the former also depends on local sequence and solvent accessibility [30]. Nevertheless, as hypothesized many of the ligand-induced changes in collective motions correspond to their vulnerability to HDX.

In the ligand free enzyme, the lowest frequency modes involve motions of the entire F-G region as well as the intervening loops of the G-H, H-I, and K"-L helices, and the B-B' loop, with the greatest temperature factors localized to the G-H and H-I regions. (Figures 5A, 6A, and S7A). In the presence of AZA, the collective motions shift to include the E-F and F-F' region (three lowest modes) as well as the H-I and K"-L loops (fourth and fifth modes). In the composite of these five modes, fluctuation of the E-F region predominates. Differences in the mode specific temperature factors derived from the AZA-bound and ligand-free CYP3A4 trajectories (Figure 6B) further highlight that collective motions of the

E-F region, F-G', and G'-G regions are enhanced in the presence of AZA. These regions are also the most deprotected from HDX by the presence of AZA. There is also enhancement of the temperature factor of the A' helix, for which deprotection was also observed at later time points. Both the G-H and H-I loops are disordered in the ligand-free and AZA-bound crystal structures of CYP3A4. Their collective motions were suppressed in the lowest frequency normal modes, although inspection of the residue-wise differences in the RMSFs show that the motions of both regions are somewhat enhanced overall, indicating that such motion is relegated to the higher frequency modes. Indeed, some deprotection of the H-I loop is observed, however the disorder and extensive solvent exposure of the G-H loop likely prevent observable differences in the G-H loop. Finally, AZA induces protection of the region linking the K helix and the third strand of β_1. While this region does not contribute to the collective motions of the lowest frequency normal modes, it interacts directly with AZA's aminothiotriazole in the dominant binding mode, thereby shielding it from solvent.

Relative to the ligand-free enzyme, RIT predominately activates fluctuations of the H-I and the K"-L loops. Accordingly, deprotection of the H-I region relative to the ligand free enzyme is observed in early time points. Due to its disorder and solvent exposure, the activation of the K"-L region does appear to confer additional deprotection to the K"-L region. RIT confers strong protection to the C-terminus of the G-helix. In agreement with the HDX measurements, fluctuations of G-helix are suppressed both in the low-frequency normal modes as well as in the residue-wise RMSF. We speculate that the RIT induced changes in the F-helix packing result in the observed protection of the E-helix from HDX. (Figure S7) As mentioned above, this is a secondary effect of RIT's interactions in the active site, most notably its direct contact with the F'-helix. The protection conferred on the β_3 hairpin cannot be explained by changes in the fluctuations; however, solvent accessible surface areas of the backbone N-H are increased (Figure S8) in the presence of RIT thereby making them vulnerable to HDX. Thus, for the different ligands there are varying levels of agreement between H/DX and normal mode effects. Together, these results lead to the likelihood that local SASA and H-bonding, as well as long range effects on tertiary packing of structural elements that dominate normal modes, all contribute to localized H/DX behavior.

Discussion

It is widely accepted that the conformational flexibility of CYP3A4 is important for its extreme ligand promiscuity, but detailed models for ligand-dependent dynamics in a membrane have until now been limited to MD simulations [5], [24]. Here, we performed HDX-MS on CYP3A4 in lipid NDs bound to six ligands to understand how the dynamics of the monomeric enzyme in a membrane bilayer respond upon binding diverse ligands. The results demonstrate that the most significant effects of ligands on CYP3A4 dynamics occur on the most flexible elements of the secondary structure that do not contact the ligands directly in the bound state. This suggests that CYP3A4 ligands differentially engage the flexible elements of the structure (C-D, E-F, G, H-I) via long-range communication pathways to be accommodated accordingly in the active site. Speculatively, this molecular mechanism is consistent with the widespread atypical kinetic of CYP3A4 often attributed to multiple ligands occupying effector and/or allosteric sites [79]–[81]. Beyond CYP3A4,

prospective key players that dictate P450 allosterism have been proposed with the majority of the functional residues residing in helices F,G, and I, the B'-C loop, and β4 sheet, though such residues were poorly conserved across P450 isoforms, alluding to the requirement for conformational flexibility [82].

Intriguingly, the HDX effect at the C-D region of CYP3A4, is most dominant for the type II ligands, RIT, and MIC. Deprotection of the C-helix was also observed for ketoconazole [22]. The HDX effects of the type II ligands at the C-D region may be functionally relevant as it has been suggested that the C-D loop contributes to the binding interface with redox partner CPR for some P450 enzymes. Based on NMR of a complex of flCYP2B4 with the flavin-binding domain of CPR in peptide 4F-lipid DMPC NDs, and previous site-directed mutagenesis, Prade *et al* reported that most of the binding surface of flCYP2B4 with the FMN domain of CPR consists of residues R133, F135, M137, and K139 in the C-D loop, along with other residues in the proximal loop near the heme [83]. More broadly, helices C and D have been shown to play a role in the docking of electron donors including Cyt b_5 to mammalian P450s [84]. The binding interaction with CPR has been studied for several mammalian P450s including CYP2B4 [83], [85], [86], and CYP2B6 [87], the specific 3A4 residues that interact with CPR have not been identified. The HDX effects at the C-D region suggest ligand-mediated modulation of dynamics at a potential interface with redox partner, CPR [88]. Although we have not measured HDX on the CYP3A4:CYPR complex, this C-D region of CYP3A4 would be expected to undergo a decrease in dynamics which would be expected to have a 'protective' effect on HDX. That is, the expected effects of CYPR are opposite to the observed effects of type II ligands. This would lead to a ligand-induced decrease in affinity for CYPR and a CYPR-dependent decrease in affinity for type II ligands, though this has yet to be experimentally validated.

While Type II ligands behave similarly, the overall HDX effects do not cleanly partition into type I or type II ligand responses. For instance, the HDX profile of TST (type I) is more like MIC (type II) than AZA or NIF (type I). In the HDX analysis of CYP3A4 in solution by Ducharme *et al*, TST had no apparent effect on the G-helix and caused protection of the F- (193–213) and F'-helices (221–226) [23]. Additional protective effects were observed at the B'-C loop (114–122), E-helix (182–189) and loop connecting to β1–4 strand (389–396). In the present work, the latter peptides exchange deuterium more slowly with ND-embedded CYP3A4 and appear unaffected by ligands. The faster exchange in solution indicates that CYP3A4 is more dynamic when removed from a membrane environment. This observation indirectly supports the gain in stability that occurs when CYP3A4 is embedded in lipid NDs [89]. Thus, the discrepancies in the HDX results of TST-bound CYP3A4 in solution and in NDs highlight the role of the lipid environment in the dynamic behavior of CYP3A4 and interactions with ligands. Lastly, several peptides in the Ducharme *et al* analysis appear bimodal, indicating greater population heterogeneity of CYP3A4 in solution, as previously observed [28].

It is notable that the HDX effects observed here are a mixture of deprotective and protective effects, with some ligands such as AZA and NIF causing almost exclusively deprotective effects. An increase in HDX relative to the free state was also the most dominant effect on CYP3A4 dynamics with midazolam [26]. Importantly, the observed increase in dynamics is

not unique to allosteric ligands such as midazolam and TST, but appears characteristic of CYP3A4 interactions with all ligands. This behavior is counterintuitive to the decrease in HDX typically observed when a ligand makes stabilizing contacts with the protein backbone [30], [90], and represents a stark contrast to the sharp decrease in HDX observed with androgen-specific cytochrome P450s [50], [91]. The native ligand androstenedione has a clear stabilizing effect on dynamics of ND-embedded aromatase (CYP19A1) that is most pronounced at the active site, access channel, and membrane interface [50]. A similar suppression of HDX with a preferred ligand has been reported for steroidogenic P450, CYP46A1, where the native ligand cholesterol suppresses HDX globally upon binding [91]. Thus, the modest and mixed effects of diverse ligands on the dynamics of CYP3A4 likely reflect the promiscuous behavior of the enzyme and its lack of preference toward any ligand.

These studies focus on dynamics of CYP3A4 for the ensemble of ligand-bound states and do not explicitly report on mechanisms by which ligands reach their final bound states. The studies were aimed to understand the equilibrium response of CYP3A4 to a wide range of structurally unrelated ligands in order to understand it's promiscuity. It is striking, however, that there is significant overlap in some regions that exhibit altered dynamics in the bound state and regions expected to provide channels for or barriers to ligand binding, including B', F, G, the B'/C loop and F/G loop [92, 93]. Promiscuity of bound states is reasonably expected to depend on promiscuity of the encounter complexes that lead to them.

The correspondence between domains most sensitive to HDX and those dominating the essential dynamics are encouraging despite several factors confounding direct comparison of the experiments and simulations. The rate and extent of HDX in proteins largely depends on the backbone solvent exposure, relative strengths of hydrogen bonds among secondary structures, and the local sequence environment. MD simulations based on fixed topology, non-polarizable force fields inform on temporal changes of the protein conformation, although hydrogen bond strengths and inferences about variations backbone amide pK_as variation are far less reliable. Even with the application of accelerated sampling methods to MD for sampling rare events, the timescales interrogated by HDX and MD still differ by several orders of magnitude. Furthermore, backbone RMSD/F typically often used to quantitate and compare protein motion present in MD trajectories are contaminated by high frequency motions that may distract from those most relevant to protein function. Filtration of high frequency motions by PCA reveals the lowest frequency eigenmodes to reveal the dynamics most essential to the protein function. Such modes occupy the lowest positions in the vibrational manifold because they involve large scale motions with the greatest mass displacements. Accordingly, their low frequencies afford the longest lifetimes to exchange competent conformations for HDX. In view of the aforementioned confounding factors, direct correlation between the normal mode-derived temperature factors and changes in HDX should not be expected. However, correspondence between those regions experiencing the greatest ligand-induced changes in HDX with those domains contributing to the essential dynamics support that HDX is indeed reporting on the most relevant functional dynamics of CYP3A4 and supports the notion that these motions are differentially perturbed by diverse ligands including increased motion far from the active site.

Supplementary Material

Refer to Web version on PubMed Central for supplementary material.

Acknowledgements:

This work was supported by National Institutes of Health grants R01GM135414 and R01GM130810 awarded to W. M. A. and J. C. H. Molecular dynamics simulations were afforded by a generous allocation of computational resources from the Ohio Supercomputer Center.

Abbreviations:

ACN	acetonitrile
ANF	α-naphthoflavone
AZA	azamulin
BEC	bromoergocriptine
CPR	cytochrome P450 reductase
CO	carbon monoxide
CV	column volume
CYP	cytochrome P450
CYP3A4	cytochrome P450 3A4
DFB	disc forming buffer
DMPC	1,2-Dimyristoyl-sn-glycero-3-phosphocholine
DT	drift time
ERY	erythromycin
FA	formic acid
FBD	flavin binding domain
GaMD	Gaussian accelerated molecular dynamics
HA	hydroxyapatite
HDX-MS	hydrogen deuterium exchange mass spectrometry
IMZ	imidazole
KPi	potassium phosphate
MIC	miconazole
MDZ	midazolam

MSP1D1	membrane scaffold protein 1D1
ND	nanodisc
NIF	nifedipine
PCA	principal component analyses
POPC	phosphatidylcholine
PR	plastic region
RIT	ritonavir
RT	retention tim
SRS	Substrate recognition site
TFA	trifluoroacetic acid
TST	testosterone

Works cited

[1]. Rendic S and Guengerich FP, “Survey of Human Oxidoreductases and Cytochrome P450 Enzymes Involved in the Metabolism of Xenobiotic and Natural Chemicals,” Chem. Res. Toxicol, vol. 28, no. 1, pp. 38–42, Jan. 2015, doi: 10.1021/TX500444E. [PubMed: 25485457]

[2]. Fernando H, Davydov DR, Chin CC, and Halpert JR, “Role of subunit interactions in P450 oligomers in the loss of homotropic cooperativity in the cytochrome P450 3A4 mutant L211F/D214E/F304W,” Arch. Biochem. Biophys, vol. 460, no. 1, pp. 129–140, Apr. 2007, doi: 10.1016/J.ABB.2006.12.025. [PubMed: 17274942]

[3]. Davydov DR, Davydova NY, Sineva EV, Kufareva I, and Halpert JR, “Pivotal role of P450-P450 interactions in CYP3A4 allostery: the case of α-naphthoflavone.,” Biochem. J, vol. 453, no. 2, pp. 219–30, 2013, doi: 10.1042/BJ20130398. [PubMed: 23651100]

[4]. Yamazaki H, Johnson WW, Ueng YF, Shimada T, and Guengerich FP, “Lack of electron transfer from cytochrome b5 in stimulation of catalytic activities of cytochrome P450 3A4: Characterization of a reconstituted cytochrome P450 3A4/NADPH-cytochrome P450 reductase system and studies with apo-cytochrome b5,” J. Biol. Chem, vol. 271, no. 44, pp. 27438–27444, 1996, doi: 10.1074/jbc.271.44.27438. [PubMed: 8910324]

[5]. Šrejber M et al. , “Membrane-attached mammalian cytochromes P450: An overview of the membrane’s effects on structure, drug binding, and interactions with redox partners,” J. Inorg. Biochem, vol. 183, pp. 117–136, Jun. 2018, doi: 10.1016/J.JINORGBIO.2018.03.002. [PubMed: 29653695]

[6]. Barnaba C, Gentry K, Sumangala N, and Ramamoorthy A, “The catalytic function of cytochrome P450 is entwined with its membrane-bound nature.,” F1000Research, vol. 6, p. 662, 2017, doi: 10.12688/f1000research.11015.1.

[7]. Barnaba C et al. , “Cytochrome-P450-Induced Ordering of Microsomal Membranes Modulates Affinity for Drugs,” Angew. Chem. - Int. Ed, vol. 57, no. 13, pp. 3391–3395, Mar. 2018, doi: 10.1002/anie.201713167.

[8]. Easterbrook J, Lu C, Sakai Y, and Li AP, “Effects of organic solvents on the activities of cytochrome P450 isoforms, UDP-dependent glucuronyl transferase, and phenol sulfotransferase in human hepatocytes,” Drug Metab. Dispos. Biol. Fate Chem, vol. 29, no. 2, pp. 141–144, Feb. 2001. [PubMed: 11159803]

[9]. Iwase M, Kurata N, Ehana R, Nishimura Y, Masamoto T, and Yasuhara H, “Evaluation of the effects of hydrophilic organic solvents on CYP3A-mediated drug-drug interaction in vitro,”

Hum. Exp. Toxicol, vol. 25, no. 12, pp. 715–721, Dec. 2006, doi: 10.1177/0960327106071979. [PubMed: 17286149]

[10]. Atkins WM, "Non-Michaelis-Menten Kinetics in Cytochrome P450-Catalyzed Reactions," Annu. Rev. Pharmacol. Toxicol, vol. 45, no. 1, pp. 291–310, 2005, doi: 10.1146/annurev.pharmtox.45.120403.100004. [PubMed: 15832445]

[11]. Nobeli I, Favia AD, and Thornton JM, "Protein promiscuity and its implications for biotechnology," Nat. Biotechnol, vol. 27, no. 2, pp. 157–167, Feb. 2009, doi: 10.1038/nbt1519. [PubMed: 19204698]

[12]. Sevrioukova IF and Poulos TL, "Structural basis for regiospecific midazolam oxidation by human cytochrome P450 3A4," Proc. Natl. Acad. Sci. U. S. A, vol. 114, no. 3, pp. 486–491, Jan. 2017, doi: 10.1073/pnas.1616198114. [PubMed: 28031486]

[13]. Yano JK, Wester MR, Schoch GA, Griffin KJ, Stout CD, and Johnson EF, "The structure of human microsomal cytochrome P450 3A4 determined by X-ray crystallography to 2.05-A resolution.," J. Biol. Chem, vol. 279, no. 37, pp. 38091–4, Sep. 2004, doi: 10.1074/jbc.C400293200. [PubMed: 15258162]

[14]. Ekroos M and Sjogren T, "Structural basis for ligand promiscuity in cytochrome P450 3A4," Proc. Natl. Acad. Sci, vol. 103, no. 37, pp. 13682–13687, 2006, doi: 10.1073/pnas.0603236103. [PubMed: 16954191]

[15]. Paulsen MD and Ornstein RL, "Dramatic differences in the motions of the mouth of open and closed cytochrome P450BM-3 by molecular dynamics simulations," Proteins, vol. 21, no. 3, pp. 237–243, Mar. 1995, doi: 10.1002/prot.340210306. [PubMed: 7784427]

[16]. Li H and Poulos TL, "The structure of the cytochrome p450BM-3 haem domain complexed with the fatty acid substrate, palmitoleic acid," Nat. Struct. Biol, vol. 4, no. 2, Art. no. 2, Feb. 1997, doi: 10.1038/nsb0297-140.

[17]. Lee Y-T, Wilson RF, Rupniewski I, and Goodin DB, "P450cam visits an open conformation in the absence of substrate," Biochemistry, vol. 49, no. 16, pp. 3412–3419, Apr. 2010, doi: 10.1021/bi100183g. [PubMed: 20297780]

[18]. Scott EE, White MA, He YA, Johnson EF, Stout CD, and Halpert JR, "Structure of mammalian cytochrome P450 2B4 complexed with 4-(4-chlorophenyl)imidazole at 1.9-A resolution: insight into the range of P450 conformations and the coordination of redox partner binding," J. Biol. Chem, vol. 279, no. 26, pp. 27294–27301, Jun. 2004, doi: 10.1074/JBC.M403349200. [PubMed: 15100217]

[19]. Zhao Y, White MA, Muralidhara BK, Sun L, Halpert JR, and Stout CD, "Structure of microsomal cytochrome P450 2B4 complexed with the antifungal drug bifonazole: insight into P450 conformational plasticity and membrane interaction," J. Biol. Chem, vol. 281, no. 9, pp. 5973–5981, Mar. 2006, doi: 10.1074/JBC.M511464200. [PubMed: 16373351]

[20]. Otyepka M, Berka K, and Anzenbacher P, "Is there a relationship between the substrate preferences and structural flexibility of cytochromes P450?," Curr. Drug Metab, vol. 13, no. 2, pp. 130–142, Jan. 2012, doi: 10.2174/138920012798918372. [PubMed: 22208528]

[21]. Hendrychová T et al. , "Flexibility of human cytochrome P450 enzymes: Molecular dynamics and spectroscopy reveal important function-related variations," Biochim. Biophys. Acta - Proteins Proteomics, vol. 1814, no. 1, pp. 58–68, Jan. 2011, doi: 10.1016/j.bbapap.2010.07.017.

[22]. Treuheit NA et al. , "Membrane Interactions, Ligand-Dependent Dynamics, and Stability of Cytochrome P4503A4 in Lipid Nanodiscs," Biochemistry, vol. 55, no. 7, pp. 1058–1069, Feb. 2016, doi: 10.1021/acs.biochem.5b01313. [PubMed: 26814638]

[23]. Ducharme J, Sevrioukova IF, Thibodeaux CJ, and Auclair K, "Structural Dynamics of Cytochrome P450 3A4 in the Presence of Substrates and Cytochrome P450 Reductase," Biochemistry, vol. 60, no. 28, pp. 2259–2271, Jul. 2021, doi: 10.1021/ACS.BIOCHEM.1C00178. [PubMed: 34196520]

[24]. Hackett JC, "Membrane-embedded substrate recognition by cytochrome P450 3A4.," J. Biol. Chem, vol. 293, no. 11, pp. 4037–4046, Jan. 2018, doi: 10.1074/jbc.RA117.000961. [PubMed: 29382727]

[25]. Davydov DR, Yang Z, Davydova N, Halpert JR, and Hubbell WL, “Conformational Mobility in Cytochrome P450 3A4 Explored by Pressure-Perturbation EPR Spectroscopy,” Biophys. J, vol. 110, no. 7, pp. 1485–1498, Apr. 2016, doi: 10.1016/j.bpj.2016.02.026. [PubMed: 27074675]

[26]. Redhair M, Hackett JC, Pelletier RD, and Atkins WM, “Dynamics and Location of the Allosteric Midazolam Site in Cytochrome P4503A4 in Lipid Nanodiscs,” Biochemistry, vol. 59, no. 6, pp. 766–779, Feb. 2020, doi: 10.1021/acs.biochem.9b01001. [PubMed: 31961139]

[27]. Park H, Lee S, and Suh J, “Structural and dynamical basis of broad substrate specificity, catalytic mechanism, and inhibition of cytochrome P450 3A4,” J. Am. Chem. Soc, vol. 127, no. 39, pp. 13634–13642, Oct. 2005, doi: 10.1021/JA053809Q/SUPPL_FILE/JA053809QSI20050804_013830.PDF. [PubMed: 16190729]

[28]. Mak PJ, Denisov IG, Grinkova YV, Sligar SG, and Kincaid JR, “Defining CYP3A4 Structural Responses to Substrate Binding. Raman Spectroscopic Studies of a Nanodisc-Incorporated Mammalian Cytochrome P450,” J. Am. Chem. Soc, vol. 133, no. 5, pp. 1357–1366, Feb. 2011, doi: 10.1021/ja105869p. [PubMed: 21207936]

[29]. Dubey KD and Shaik S, “Cytochrome P450-The Wonderful Nanomachine Revealed through Dynamic Simulations of the Catalytic Cycle,” Acc. Chem. Res, vol. 52, no. 2, pp. 389–399, Feb. 2019, doi: 10.1021/ACS.ACCOUNTS.8B00467. [PubMed: 30633519]

[30]. Konermann L, Pan J, and Liu Y-H, “Hydrogen exchange mass spectrometry for studying protein structure and dynamics,” Chem Soc Rev, vol. 40, no. 3, pp. 1224–1234, Feb. 2011, doi: 10.1039/C0CS00113A. [PubMed: 21173980]

[31]. Masson GR et al. , “Recommendations for performing, interpreting and reporting hydrogen deuterium exchange mass spectrometry (HDX-MS) experiments,” Nat. Methods, vol. 16, no. 7, pp. 595–602, 2019, doi: 10.1038/s41592-019-0459-y. [PubMed: 31249422]

[32]. “Ritonavir | C37H48N6O5S2 - PubChem.” https://pubchem.ncbi.nlm.nih.gov/compound/392622 (accessed Jan. 11, 2022).

[33]. Sevrioukova IF and Poulos TL, “Structure and mechanism of the complex between cytochrome P4503A4 and ritonavir,” Proc. Natl. Acad. Sci. U. S. A, vol. 107, no. 43, pp. 18422–18427, Oct. 2010, doi: 10.1073/PNAS.1010693107. [PubMed: 20937904]

[34]. Ernest CS, Hall SD, and Jones DR, “Mechanism-Based Inactivation of CYP3A by HIV Protease Inhibitors,” J. Pharmacol. Exp. Ther, vol. 312, no. 2, pp. 583–591, Feb. 2005, doi: 10.1124/JPET.104.075416. [PubMed: 15523003]

[35]. “Nifedipine | C17H18N2O6 - PubChem.” https://pubchem.ncbi.nlm.nih.gov/compound/4485 (accessed Jan. 11, 2022).

[36]. “Bromocriptine | C32H40BrN5O5 - PubChem.” https://pubchem.ncbi.nlm.nih.gov/compound/31101 (accessed Jan. 11, 2022).

[37]. Sevrioukova IF and Poulos TL, “Structural and Mechanistic Insights into the Interaction of Cytochrome P4503A4 with Bromoergocryptine, a Type I Ligand,” J. Biol. Chem, vol. 287, no. 5, p. 3510, Jan. 2012, doi: 10.1074/JBC.M111.317081. [PubMed: 22157006]

[38]. “Azamulin | C24H38N4O4S - PubChem.” https://pubchem.ncbi.nlm.nih.gov/compound/16072188 (accessed Jan. 11, 2022).

[39]. Sevrioukova IF, “Structural Insights into the Interaction of Cytochrome P450 3A4 with Suicide Substrates: Mibefradil, Azamulin and 6’,7’-Dihydroxybergamottin,” Int. J. Mol. Sci, vol. 20, no. 17, Sep. 2019, doi: 10.3390/IJMS20174245.

[40]. “Testosterone | C19H28O2 - PubChem.” https://pubchem.ncbi.nlm.nih.gov/compound/6013 (accessed Jan. 11, 2022).

[41]. Kenworthy KE, Clarke SE, Andrews J, and Houston JB, “Multisite Kinetic Models for Cyp3a4 : Simultaneous Activation and Inhibition of Diazepam and Testosterone Metabolism Abstract :,” Drug Metab. Dispos, vol. 29, no. 12, pp. 1644–1651, 2001. [PubMed: 11717184]

[42]. Nath A, Grinkova YV, Sligar SG, and Atkins WM, “Ligand binding to cytochrome P450 3A4 in phospholipid bilayer nanodiscs: the effect of model membranes.,” J. Biol. Chem, vol. 282, no. 39, pp. 28309–20, Sep. 2007, doi: 10.1074/jbc.M703568200. [PubMed: 17573349]

[43]. Woods CM, Fernandez C, Kunze KL, and Atkins WM, “Allosteric Activation of Cytochrome P450 3A4 by α-Naphthoflavone: Branch Point Regulation Revealed by Isotope Dilution

Analysis," Biochemistry, vol. 50, no. 46, p. 10041, 2011, doi: 10.1021/BI2013454. [PubMed: 22004098]

[44]. Baas BJ, Denisov IG, and Sligar SG, "Homotropic cooperativity of monomeric cytochrome P450 3A4 in a nanoscale native bilayer environment," Arch. Biochem. Biophys, vol. 430, no. 2, pp. 218–228, 2004, doi: 10.1016/j.abb.2004.07.003. [PubMed: 15369821]

[45]. "Nanodisc Technology: Protocols for Preparation of Nanodiscs | Sligar Lab." https://publish.illinois.edu/sligar-lab/nanodisc-technology-protocols-for-preparation-of-nanodiscs/ (accessed Jan. 04, 2022).

[46]. Gillam EMJ, Baba T, Kim BR, Ohmori S, and Guengerich FP, "Expression of modified human cytochrome P450 3A4 in Escherichia coli and purification and reconstitution of the enzyme," Arch. Biochem. Biophys, vol. 305, no. 1, pp. 123–131, 1993, doi: 10.1006/ABBI.1993.1401. [PubMed: 8342945]

[47]. OMURA T and SATO R, "THE CARBON MONOXIDE-BINDING PIGMENT OF LIVER MICROSOMES. I. EVIDENCE FOR ITS HEMOPROTEIN NATURE.," J. Biol. Chem, vol. 239, pp. 2370–8, Jul. 1964. [PubMed: 14209971]

[48]. Hebling CM, Morgan CR, Stafford DW, Jorgenson JW, Rand KD, and Engen JR, "Conformational analysis of membrane proteins in phospholipid bilayer nanodiscs by hydrogen exchange mass spectrometry," Anal. Chem, vol. 82, no. 13, pp. 5415–5419, Jul. 2010, doi: 10.1021/AC100962C. [PubMed: 20518534]

[49]. Murphree TA, Vorauer C, Brzoska M, and Guttman M, "Imidazolium Compounds as Internal Exchange Reporters for Hydrogen/Deuterium Exchange by Mass Spectrometry," Anal. Chem, vol. 92, no. 14, pp. 9830–9837, Jul. 2020, doi: 10.1021/ACS.ANALCHEM.0C01328. [PubMed: 32569457]

[50]. Paço L, Zarate-Perez F, Clouser AF, Atkins WM, and Hackett JC, "Dynamics and Mechanism of Binding of Androstenedione to Membrane-Associated Aromatase," Biochemistry, vol. 59, no. 33, pp. 2999–3009, Aug. 2020, doi: 10.1021/acs.biochem.0c00460. [PubMed: 32786398]

[51]. Guttman M, Weis DD, Engen JR, and Lee KK, "Analysis of overlapped and noisy hydrogen/deuterium exchange mass spectra," J. Am. Soc. Mass Spectrom, vol. 24, no. 12, pp. 1906–1912, Dec. 2013, doi: 10.1007/s13361-013-0727-5. [PubMed: 24018862]

[52]. Möller IR et al. , "Improving the Sequence Coverage of Integral Membrane Proteins during Hydrogen/Deuterium Exchange Mass Spectrometry Experiments," Anal. Chem, vol. 91, no. 17, pp. 10970–10978, Sep. 2019, doi: 10.1021/ACS.ANALCHEM.9B00973. [PubMed: 31408320]

[53]. Webb B and Sali A, "Comparative Protein Structure Modeling Using MODELLER," Curr. Protoc. Bioinforma, vol. 54, p. 5.6.1–5.6.37, Jun. 2016, doi: 10.1002/cpbi.3.

[54]. Lomize MA, Pogozheva ID, Joo H, Mosberg HI, and Lomize AL, "OPM database and PPM web server: resources for positioning of proteins in membranes," Nucleic Acids Res, vol. 40, no. Database issue, pp. D370–376, Jan. 2012, doi: 10.1093/nar/gkr703. [PubMed: 21890895]

[55]. Jo S, Kim T, Iyer VG, and Im W, "CHARMM-GUI: a web-based graphical user interface for CHARMM," J. Comput. Chem, vol. 29, no. 11, pp. 1859–1865, Aug. 2008, doi: 10.1002/jcc.20945. [PubMed: 18351591]

[56]. Phillips JC et al. , "Scalable molecular dynamics with NAMD," J. Comput. Chem, vol. 26, no. 16, pp. 1781–1802, Dec. 2005, doi: 10.1002/jcc.20289. [PubMed: 16222654]

[57]. Huang J et al. , "CHARMM36m: an improved force field for folded and intrinsically disordered proteins," Nat. Methods, vol. 14, no. 1, pp. 71–73, Jan. 2017, doi: 10.1038/nmeth.4067. [PubMed: 27819658]

[58]. Vanommeslaeghe K and MacKerell AD, "Automation of the CHARMM General Force Field (CGenFF) I: bond perception and atom typing," J. Chem. Inf. Model, vol. 52, no. 12, pp. 3144–3154, Dec. 2012, doi: 10.1021/ci300363c. [PubMed: 23146088]

[59]. Martyna GJ, Tobias DJ, and Klein ML, "Constant pressure molecular dynamics algorithms," J. Chem. Phys, vol. 101, no. 5, pp. 4177–4189, Sep. 1994, doi: 10.1063/1.467468.

[60]. Feller SE, Zhang Y, Pastor RW, and Brooks BR, "Constant pressure molecular dynamics simulation: The Langevin piston method," J. Chem. Phys, vol. 103, no. 11, pp. 4613–4621, Sep. 1995, doi: 10.1063/1.470648.

[61]. Wang A, Stout CD, Zhang Q, and Johnson EF, “Contributions of ionic interactions and protein dynamics to cytochrome P450 2D6 (CYP2D6) substrate and inhibitor binding,” J. Biol. Chem, vol. 290, no. 8, pp. 5092–5104, Feb. 2015, doi: 10.1074/JBC.M114.627661. [PubMed: 25555909]

[62]. Pang YT, Miao Y, Wang Y, and McCammon JA, “Gaussian Accelerated Molecular Dynamics in NAMD,” J. Chem. Theory Comput, vol. 13, no. 1, pp. 9–19, Jan. 2017, doi: 10.1021/acs.jctc.6b00931. [PubMed: 28034310]

[63]. Matsunaga Y and Sugita Y, “Refining Markov state models for conformational dynamics using ensemble-averaged data and time-series trajectories,” J. Chem. Phys, vol. 148, no. 24, p. 241731, Jun. 2018, doi: 10.1063/1.5019750. [PubMed: 29960305]

[64]. Mitternacht S, “FreeSASA: An open source C library for solvent accessible surface area calculations,” F1000Research, vol. 5, p. 189, 2016, doi: 10.12688/f1000research.7931.1.

[65]. Lee B and Richards FM, “The interpretation of protein structures: estimation of static accessibility,” J. Mol. Biol, vol. 55, no. 3, pp. 379–400, Feb. 1971, doi: 10.1016/0022-2836(71)90324-x. [PubMed: 5551392]

[66]. Tsai J, Taylor R, Chothia C, and Gerstein M, “The packing density in proteins: standard radii and volumes,” J. Mol. Biol, vol. 290, no. 1, pp. 253–266, Jul. 1999, doi: 10.1006/jmbi.1999.2829. [PubMed: 10388571]

[67]. Kan Z-Y, Walters BT, Mayne L, and Englander SW, “Protein hydrogen exchange at residue resolution by proteolytic fragmentation mass spectrometry analysis,” Proc. Natl. Acad. Sci. U. S. A, vol. 110, no. 41, pp. 16438–16443, Oct. 2013, doi: 10.1073/pnas.1315532110. [PubMed: 24019478]

[68]. Dai D et al., “Identification of Variants of CYP3A4 and Characterization of Their Abilities to Metabolize Testosterone and Chlorpyrifos.” Accessed: Jun. 03, 2020. [Online]. Available: http://jpet.aspetjournals.org

[69]. Zhou X-Y et al. , “Enzymatic Activities of CYP3A4 Allelic Variants on Quinine 3-Hydroxylation In Vitro,” Front. Pharmacol, vol. 10, p. 591, May 2019, doi: 10.3389/fphar.2019.00591. [PubMed: 31214030]

[70]. Sevrioukova IF, “High-Level Production and Properties of the Cysteine-Depleted Cytochrome P450 3A4,” Biochemistry, vol. 56, no. 24, pp. 3058–3067, Jun. 2017, doi: 10.1021/ACS.BIOCHEM.7B00334. [PubMed: 28590129]

[71]. Zhao Y, White MA, Muralidhara BK, Sun L, Halpert JR, and Stout CD, “Structure of Microsomal Cytochrome P450 2B4 Complexed with the Antifungal Drug Bifonazole,” J. Biol. Chem, vol. 281, no. 9, pp. 5973–5981, Mar. 2006, doi: 10.1074/jbc.M511464200. [PubMed: 16373351]

[72]. Cojocaru V, Winn PJ, and Wade RC, “The ins and outs of cytochrome P450s,” Biochim. Biophys. Acta BBA - Gen. Subj, vol. 1770, no. 3, pp. 390–401, Mar. 2007, doi: 10.1016/j.bbagen.2006.07.005.

[73]. Fishelovitch D, Shaik S, Wolfson HJ, and Nussinov R, “Theoretical characterization of substrate access/exit channels in the human cytochrome P450 3A4 enzyme: involvement of phenylalanine residues in the gating mechanism.,” J. Phys. Chem. B, vol. 113, no. 39, pp. 13018–25, Oct. 2009, doi: 10.1021/jp810386z. [PubMed: 19728720]

[74]. Gotoh O, “Substrate recognition sites in cytochrome P450 family 2 (CYP2) proteins inferred from comparative analyses of amino acid and coding nucleotide sequences.,” J. Biol. Chem, vol. 267, no. 1, pp. 83–90, Jan. 1992, doi: 10.1016/S0021-9258(18)48462-1. [PubMed: 1730627]

[75]. Paloncýová M, Navrátilová V, Berka K, Laio A, and Otyepka M, “Role of Enzyme Flexibility in Ligand Access and Egress to Active Site: Bias-Exchange Metadynamics Study of 1,3,7-Trimethyluric Acid in Cytochrome P450 3A4,” J. Chem. Theory Comput, vol. 12, no. 4, pp. 2101–2109, Apr. 2016, doi: 10.1021/ACS.JCTC.6B00075/SUPPL_FILE/CT6B00075_SI_002.ZIP. [PubMed: 26967371]

[76]. Skar-Gislinge N et al., “Small-angle scattering determination of the shape and localization of human cytochrome P450 embedded in a phospholipid nanodisc environment”, doi: 10.1107/S1399004715018702.

[77]. Berka K, Paloncýová M, Anzenbacher P, and Otyepka M, “Behavior of human cytochromes P450 on lipid membranes,” J. Phys. Chem. B, vol. 117, no. 39, pp. 11556–11564, Oct. 2013, doi: 10.1021/JP4059559. [PubMed: 23987570]

[78]. David CC and Jacobs DJ, “Principal component analysis: a method for determining the essential dynamics of proteins,” Methods Mol. Biol. Clifton NJ, vol. 1084, pp. 193–226, 2014, doi: 10.1007/978-1-62703-658-0_11.

[79]. Dabrowski MJ, Schrag ML, Wienkers LC, and Atkins WM, “Pyrene-pyrene complexes at the active site of cytochrome P450 3A4: evidence for a multiple sustrate binding site,” J. Am. Chem. Soc, vol. 124, pp. 11866–11867, 2002. [PubMed: 12358527]

[80]. Atkins WM, “Current views on the fundamental mechanisms of cytochrome P450 allosterism.,” Expert Opin. Drug Metab. Toxicol, vol. 2, no. 4, pp. 573–579, 2006, doi: 10.1517/17425255.2.4.573. [PubMed: 16859405]

[81]. Williams P. a, “Crystal Structures of Human Cytochrome P450 3A4 Bound to Metyrapone and Progesterone,” Science, vol. 305, no. 5684, pp. 683–686, 2004, doi: 10.1126/science.1099736. [PubMed: 15256616]

[82]. Hlavica P, “Challenges in assignment of allosteric effects in cytochrome P450-catalyzed substrate oxidations to structural dynamics in the hemoprotein architecture,” J. Inorg. Biochem, vol. 167, pp. 100–115, Feb. 2017, doi: 10.1016/j.jinorgbio.2016.11.025. [PubMed: 27919007]

[83]. Prade E et al. , “A Minimal Functional Complex of Cytochrome P450 and FBD of Cytochrome P450 Reductase in Nanodiscs,” Angew. Chem. Int. Ed Engl, vol. 57, no. 28, pp. 8458–8462, Jul. 2018, doi: 10.1002/ANIE.201802210. [PubMed: 29722926]

[84]. Hlavica P, “Mechanistic basis of electron transfer to cytochromes p450 by natural redox partners and artificial donor constructs,” Adv. Exp. Med. Biol, vol. 851, pp. 247–297, Jan. 2015, doi: 10.1007/978-3-319-16009-2_10. [PubMed: 26002739]

[85]. Kenaan C, Zhang H, Shea EV, and Hollenberg PF, “Uncovering the role of hydrophobic residues in cytochrome P450-cytochrome P450 reductase interactions,” Biochemistry, vol. 50, no. 19, pp. 3957–3967, May 2011, doi: 10.1021/BI1020748. [PubMed: 21462923]

[86]. Gentry KA, Anantharamaiah GM, and Ramamoorthy A, “Probing protein-protein and protein-substrate interactions in the dynamic membrane-associated ternary complex of cytochromes P450,: B 5, and reductase,” Chem. Commun, vol. 55, no. 89, pp. 13422–13425, 2019, doi: 10.1039/c9cc05904k.

[87]. Bumpus NN and Hollenberg PF, “Cross-linking of human cytochrome P450 2B6 to NADPH-cytochrome P450 reductase: Identification of a potential site of interaction,” J. Inorg. Biochem, vol. 104, no. 4, pp. 485–488, Apr. 2010, doi: 10.1016/J.JINORGBIO.2009.12.017. [PubMed: 20096935]

[88]. Pochapsky TC, “A dynamic understanding of cytochrome P450 structure and function through solution NMR,” Curr. Opin. Biotechnol, vol. 69, pp. 35–42, Jun. 2021, doi: 10.1016/j.copbio.2020.11.007. [PubMed: 33360373]

[89]. McClary WD, Sumida JP, Scian M, Paço L, and Atkins WM, “Membrane Fluidity Modulates Thermal Stability and Ligand Binding of Cytochrome P4503A4 in Lipid Nanodiscs,” Biochemistry, vol. 55, no. 45, pp. 6258–6268, Nov. 2016, doi: 10.1021/acs.biochem.6b00715. [PubMed: 27782404]

[90]. Chalmers MJ, Busby SA, Pascal BD, West GM, and Griffin PR, “Differential hydrogen/deuterium exchange mass spectrometry analysis of protein–ligand interactions,” Expert Rev. Proteomics, vol. 8, no. 1, p. 43, Feb. 2011, doi: 10.1586/EPR.10.109. [PubMed: 21329427]

[91]. Anderson KW, Mast N, Hudgens JW, Lin JB, Turko IV, and Pikuleva IA, “Allosteric site in CYP46A1 Cholesterol Hydroxylase CYP46A1: Mapping of the Allosteric Site for Efavirenz, a Drug that Stimulates Enzyme Activity,” 2016, doi: 10.1074/jbc.M116.723577.

[92]. Cojocaru V, Winn PJ, Wade RC. “The ins and outs of cytochrome P450s.” Biochim Biophys Acta. 2007 Mar;1770(3):390–401. doi: 10.1016/j. [PubMed: 16920266]

[93]. Fishelovitch D, Shaik S, Wolfson HJ, Nussinov R. Theoretical characterization of substrate access/exit channels in the human cytochrome P450 3A4 enzyme: involvement of phenylalanine residues in the gating mechanism. J Phys Chem B. 2009 Oct 1;113(39):13018–25. doi: 10.1021/jp810386z. [PubMed: 19728720]

HIGHLIGHTS

- CYP3A4 is a highly promiscuous detoxication enzyme.
- H/DX MS reveals CYP3A4 ligands cause globally distributed changes in dynamics.
- Results are supported by MD simulations and principle component analysis.
- Ligands induce an *increase* in local dynamics far from the binding site.

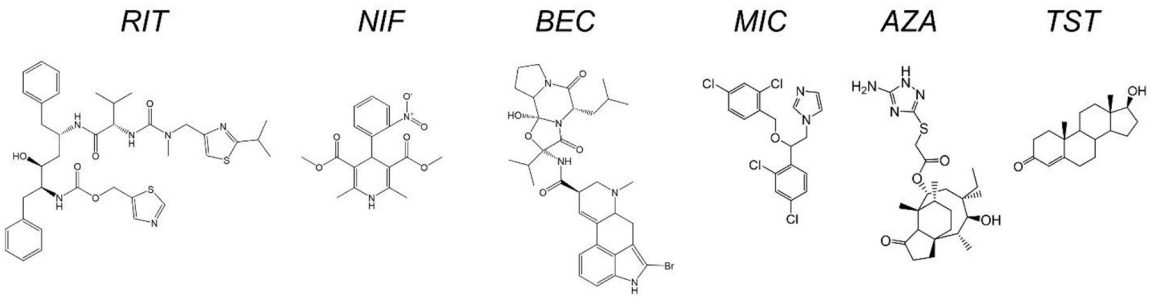

Figure 1.
Structures of CYP3A4 ligands analyzed by HDX-MS.

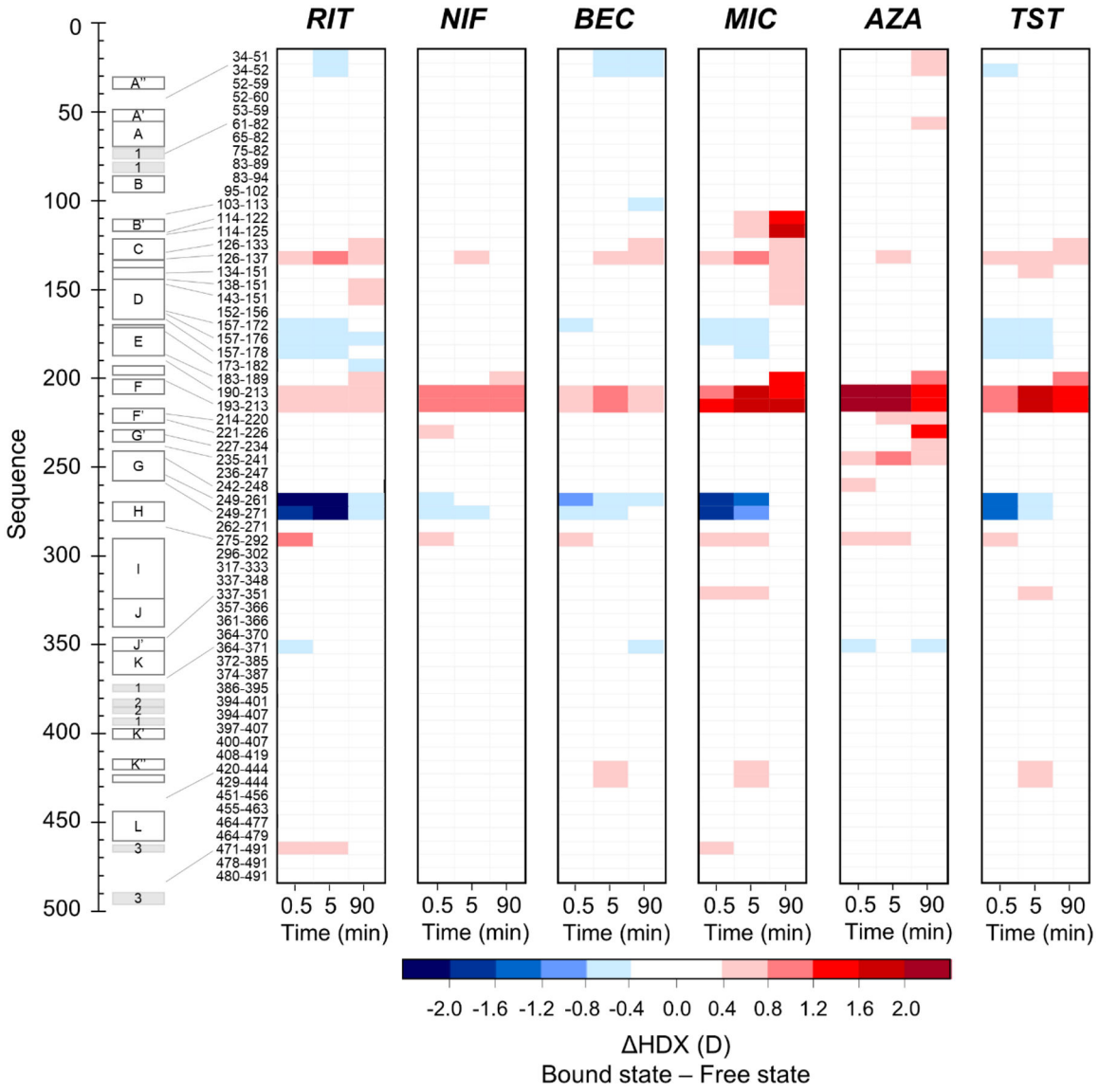

Figure 2. Chiclet plot of HDX differences between the bound and free states.

Location of the peptides that display a significant difference in HDX is shown onto the primary CYP3A4 sequence on the left. The beta sheets are shaded gray.

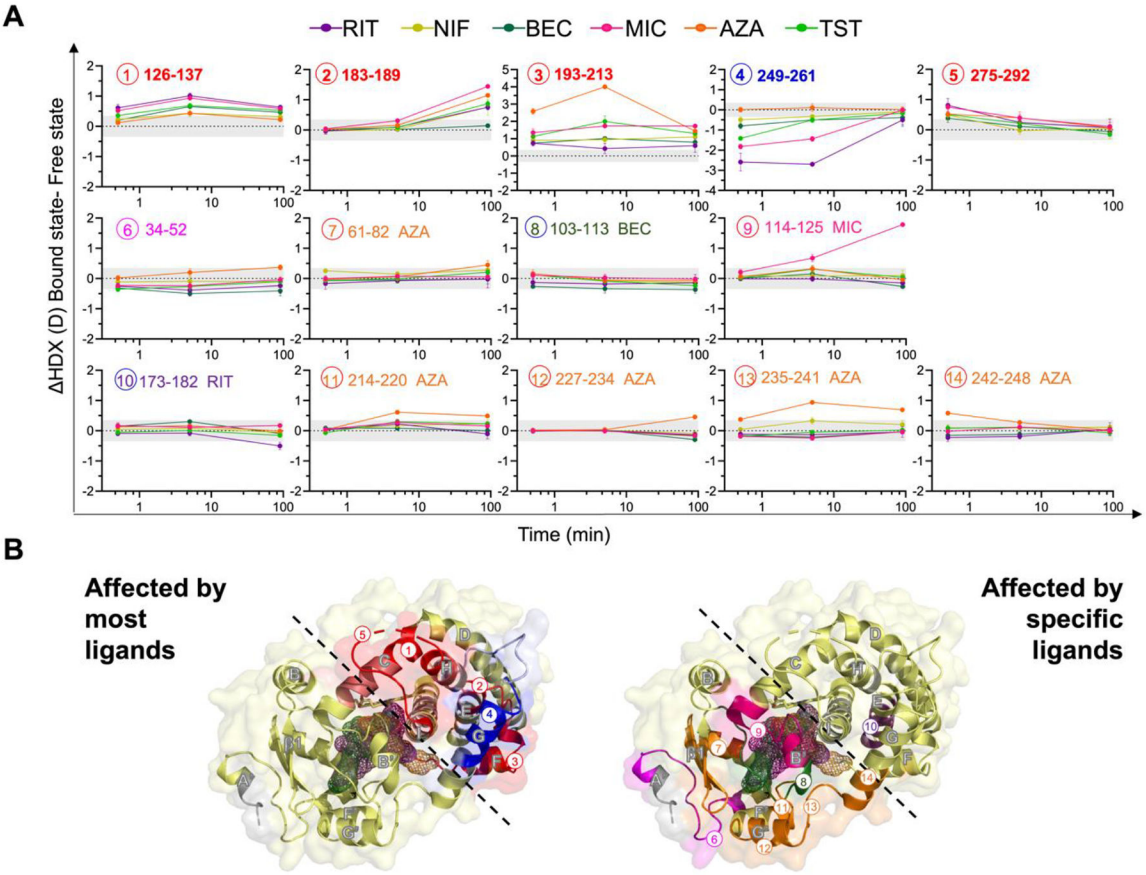

Figure 3. Common vs. unique HDX effects.

A. ΔHDX plots of peptides affected by at least five ligands (in bold), or one ligand. **B**. Peptides in A mapped onto the crystal structure of CYP3A4 (PDB: 1TQN) represented as a pale-yellow surface and partially visible cartoon. BEC, RIT and AZA are represented as a mesh surface in the active site in dark green, purple and orange, respectively. Uncovered regions are shaded gray. Commonly affected peptides (left) are shaded in red if deprotected and in blue if protected. Peptide 34–52 is in magenta as it is protected for some ligands and deprotected with others. Uniquely affected peptides (right) are shaded according to the color scheme used for each ligand in A.

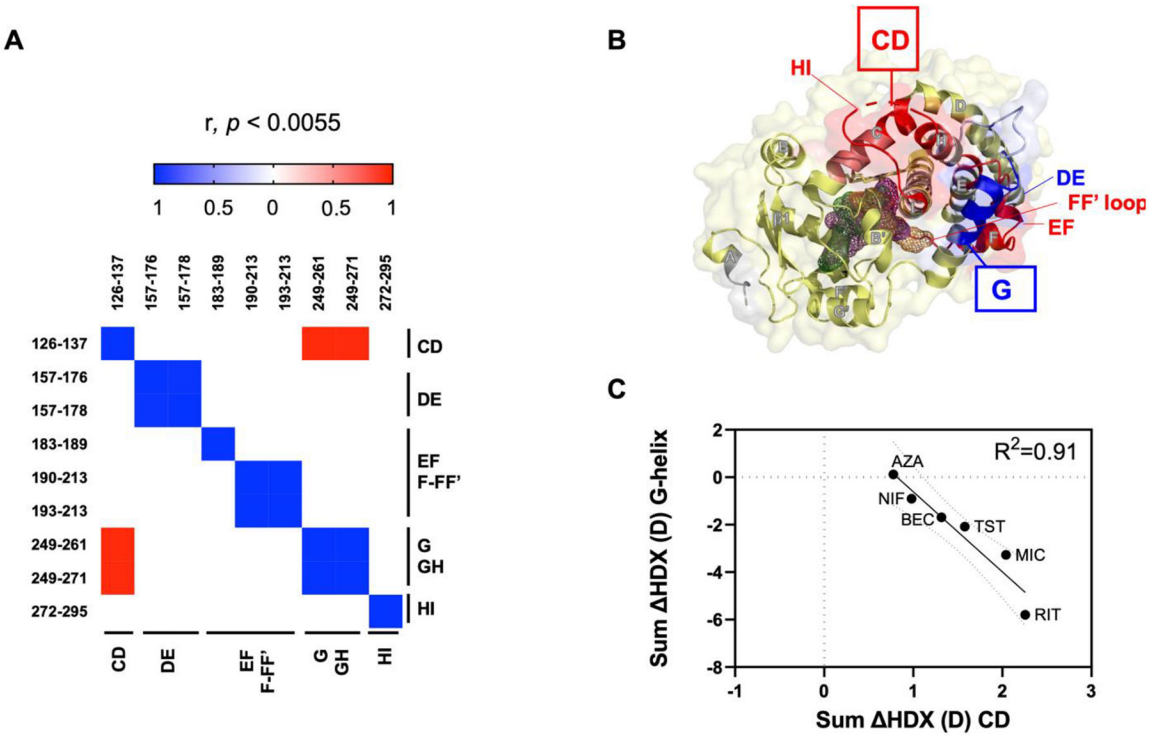

Figure 4. Dynamics of the G-helix are correlated to the C-D region.

A. Correlation matrix heatmap of sum ΔHDX at 30 s, 5 m, and 90 m for peptides that show a significant difference in HDX for at least five ligands. **B.** Peptides in **A** mapped onto the 1TQN structure (yellow) in the same color representation as in Figure 3. Only parts of the structure are visible for clarity. The C-D region and G-helix peptides are highlighted with red and blue boxes, respectively. C) Correlation plot of the sum ΔHDX of the C-D region (peptide 126–137) against the sum ΔHDX of the G-helix (peptide 249–261). Dotted lines represent the 95% CI.

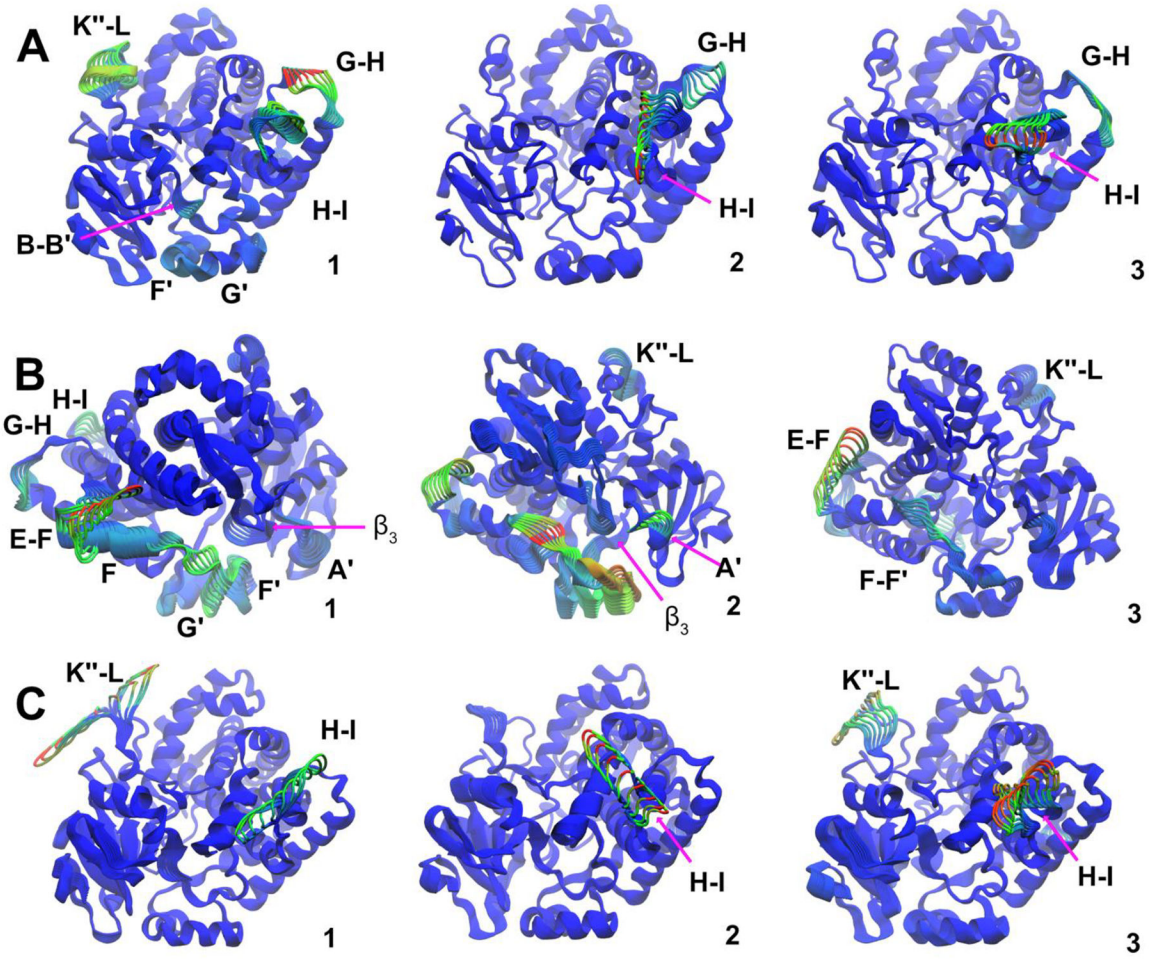

Figure 5.

Superimposed ribbon diagrams propagated along the first, second, and third normal modes of (A) ligand-free, (B) AZA-, and (C) RIT-bound CYP3A4. Structures are colored from blue to green to red based on the normalized temperature factor calculated as described in the Materials and Methods with $c = 3$.

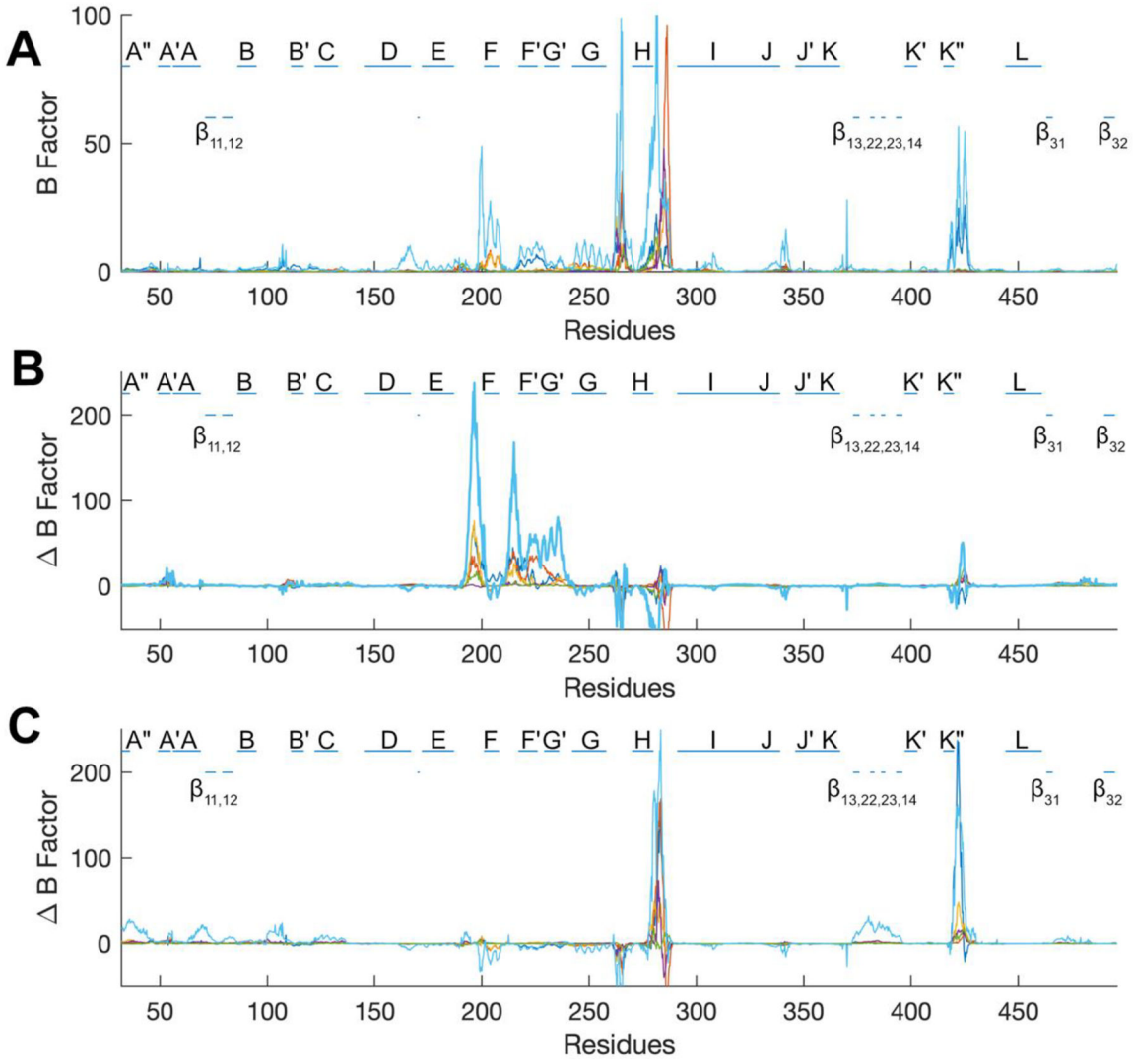

Figure 6.

(A) Projection of the vector describing the fluctuations of an amino acid (ligand) during MD simulations on the vector described by the first five normal modes. (B) Temperature factors for AZA-bound CYP3A4 less those of the ligand free enzyme. (C) Temperature factors for RIT-bound CYP3A4 less those for the ligand free enzyme. Temperature factors associated with the first five normal modes are depicted as blue, orange, yellow, purple and green lines, respectively. The temperature factor associated with the composite fluctuations of the first five normal modes are illustrated with pale blue lines.

Table 1.

Properties of CYP3A4 ligands analyzed by HDX-MS.

Ligand	Type	Affinity (μM)	X-ray structure?	Binding to CYP3A4
RIT	II	0.85	Yes	Complex: binding is stoichiometric, irreversible and biphasic. [37], [38]
NIF	I	20 *	No	Complex: multiple binder, substrate inhibition kinetics [39]
BEC	I	0.45	Yes	Single binder [40], [41]
MIC	II	0.45 *†	No	Single binder? [41]
AZA	I	1.7 *	Yes	Single binder [42]
TST	I	120 †	No	Complex: multiple binder, allosteric [28]

Kd, Ks*, † CYP3A4 in ND.